# MXene-Derived Oxide Nano-heterostructures for Photocatalytic Sulfamethoxazole Degradation

Shalu Atri, <sup>a,b\*</sup> Elham Loni, <sup>b</sup> Frantisek Zazimal, <sup>c</sup> Karol Hensel, <sup>d</sup> Maria Caplovicova, <sup>e</sup> Gustav Plesch, <sup>a</sup> Xin Lu, <sup>b</sup> Rajamani Nagarajan, <sup>f</sup> Michael Naguib, <sup>b,g\*</sup> Olivier Monfort <sup>a\*</sup>

- <sup>a</sup> Department of Inorganic Chemistry, Faculty of Natural Sciences, Comenius University, Ilkovicova 6, Mlynska dolina, 84215 Bratislava, Slovakia
- <sup>b</sup> Department of Physics and Engineering Physics, Tulane University, New Orleans, Louisiana, United States of America
- <sup>c</sup> Department of Plasma Physics and Technology, Faculty of Science Masaryk University, Masaryk University, Kotlarska 267/2, 611 37 Brno, Czechia
- <sup>d</sup> Division of Environmental Physics, Faculty of Mathematics Physics and Informatics, Comenius University, Mlynska dolina, 84248 Bratislava, Slovakia
- <sup>e</sup> STU Center for Nanodiagnostics, Faculty of Materials Science and Technology in Trnava, Slovak Technical University, Vazovova 5, 81243 Bratislava, Slovakia.
- <sup>f</sup> Materials Chemistry Group, Department of Chemistry, University of Delhi, Delhi- 110007, India
- <sup>g</sup> Department of Chemistry, Tulane University, New Orleans, Louisiana, United States of America

\*Corresponding authors: <u>shalu1@uniba.sk</u> (SA); <u>naguib@tulane.edu</u> (MN); monfort1@uniba.sk (OM)

**Abstract** 

Herein, we report for the first time the use of ternary oxide nano-heterostructure photocatalysts

derived from (Nb<sub>v</sub>, Ti<sub>1-v</sub>)<sub>2</sub>CT<sub>x</sub> MXene in the treatment of water. Three different compositions

of binary MXenes, viz.,  $(Ti_{0.75}Nb_{0.25})_2CT_x$ ,  $(Ti_{0.5}Nb_{0.5})_2CT_x$ , and  $(Ti_{0.25}Nb_{0.75})_2CT_x$  (with  $T_x =$ 

OH, F and Cl) were used as single source precursor to produce TiNbO<sub>x</sub>-3:1, TiNbO<sub>x</sub>-1:1,

TiNbO<sub>x</sub>-1:3 by controlled-atmosphere thermal oxidation. Phase identification and Le Bail

refinements confirmed the presence of a mixture of rutile TiO<sub>2</sub> and monoclinic Ti<sub>2</sub>Nb<sub>10</sub>O<sub>29</sub>.

Morphological investigations through scanning and transmission electron microscopies

revealed the retention of layered nanostructures from the MXenes precursors and the fusion of

TiO<sub>2</sub> and Ti<sub>2</sub>Nb<sub>10</sub>O<sub>29</sub> nanoparticles in forming nanosheets. Among the three oxide

nanoheterostructures, TiNbO<sub>x</sub>-3:1 exhibited the best photocatalytic performance by the

removal of 83% of sulfamethoxazole (SMX) after 2 h reaction. Such a result is explained by a

complex influence of structural, morphological, and electronic properties since TiNbO<sub>x</sub>-3:1

consisted of small-sized crystallites (40-70 nm) and possessed a higher surface area. The

suggested electronic band structure is a type-II heterojunction where recombination of

electrons and holes is minimized during photocatlytic reactions. The photocatalytic

degradation of SMX was promoted by the attack of 'OH, as evidenced by the detection of

2.2 µM of 'OH, using coumarin as probe. This study highlights the potential application of

MXene-derived oxide nano-heterostructures in wastewaters treatment.

**Keywords:** Binary MXene; Photocatalyst; Sulfamethoxazole; Wastewaters treatment; TiNbO<sub>x</sub>

Introduction

Heterogeneous photocatalysis is one of the most investigated solar conversion processes, and

it has the potential to fulfill the global need for sustainability. It is a cost-effective and

2

environment-friendly technology for wastewater treatment and production of clean energy, for example, to produce hydrogen from water splitting, <sup>2,3</sup> CO<sub>2</sub> conversion into valuable chemicals, <sup>4,5</sup> and degradation of organic pollutants. <sup>6,7</sup> Numerous photocatalysts, such as transition metal oxides, sulfides, nitrides, and many more, have been explored for water or air treatment. <sup>2-8</sup> Concerning water treatment, the continuous stress of harmful pharmaceutical active compounds (PACs) on the water bodies is an environmental problem of high concern for human and animal life. <sup>9</sup> Sulfamethoxazole (SMX) is widely used as a sulfonamide antibiotic and one of the most frequently detected PACs in wastewater from pharmaceutical companies and municipalities. <sup>10</sup> Due to the high chemical stability and poor biodegradability of SMX, conventional methods are inefficient in eliminating SMX.

Titanium dioxide (TiO<sub>2</sub>) has been proven as an efficient photocatalyst, but it is only active under the UVA spectrum due to the mismatch between its energy band gap (E<sub>g</sub>) and the solar spectrum, which contains only about 5% of UVA irradiation. This issue has originated thousands of research articles dealing with dozens of different approaches, including morphological and composition modifications to enhance the photocatalytic efficiency of TiO<sub>2</sub>. One of these approaches is to design nano-heterostructure materials, as they offer higher light harvesting properties and effectiveness in retarding the recombination of charge carriers. This phenomenon occurs due to unequal Fermi levels of the two components that allow the transport of electrons at the coupling interface. Therefore, the separation and migration of charge carriers can be enhanced.

MXenes with the  $M_{n+1}X_nT_x$  formula (M: early transition metal, X: C and/or N,  $T_x$ : functional groups,  $n = 1-4)^{17}$  are 2D multilayered materials that recently emerged as cocatalysts for photocatalytic applications due to their unique structural and electronic properties. As photocatalysts, the formation of MXene-derived transition metal oxides (MO<sub>x</sub>) can be highly efficient nanomaterials for photocatalytic applications. MXene-derived MO<sub>x</sub> are obtained

by partial or complete oxidation of MXene (Ti<sub>3</sub>C<sub>2</sub>T<sub>x</sub> and Ti<sub>2</sub>CT<sub>x</sub>) depending on oxidation conditions, and they exhibit superior properties compared to MO<sub>x</sub>/MXene composites.<sup>22,23</sup> Recent advancements in MXene-based photocatalysts highlight their growing significance in environmental and energy challenges, and ongoing research aims to overcome the current limitations and scale up their production for practical applications. 24-27 Reported studies pointed out that oxygen-containing functional groups, especially, facilitate the formation of MO<sub>x</sub> phases.<sup>28</sup> It has been reported that TiO<sub>2</sub>/amorphous carbon sheets can be derived by using flash-heating multilayer  $Ti_3C_2T_x$  in air.<sup>29</sup> The use of MXene as the precursor to produce oxide material is promising since it provides unique 2D structure, morphology, and electronic properties that cannot be achieved by employing other synthetic routes. <sup>30,31</sup> Such properties are the key factors in tuning and enhancing the photocatalytic behavior of a material. 32,33 Taking cognizance of other reported studies, the current work is focused on designing a new type of nano-heterostructure oxide photocatalysts derived from (Nb<sub>v</sub>Ti<sub>1-v</sub>)<sub>2</sub>CT<sub>x</sub> MXene as a precursor (Figure 1), since they can exhibit superior physiochemical properties than other Ti and Nb oxide composites. 34,35 Indeed, retaining the layered structure of the MXene is an innovative direction to obtain more efficient photocatalyst for the degradation of organic pollutants in water. In addition, Nb-substituted binary MXene has been used as the precursor for the first time. The selection of Nb was based on the possibility to tune the electronic properties of the resulting oxide nano-heterostructure photocatalyst. 36,37 Such a methodology has never been tested yet. Three oxide nano-heterostructures (TiNbO<sub>x</sub>) have been prepared i.e., (i) one with equal nominal amount of Ti and Nb, (ii) one with predominant Ti oxide phase, and (iii) one with predominant Nb oxide phase. A relationship between the photocatalytic activity of such innovative materials and their corresponding properties, including the crystalline phase, composition, morphology, surface chemistry, and electronic band structure, has been also presented.

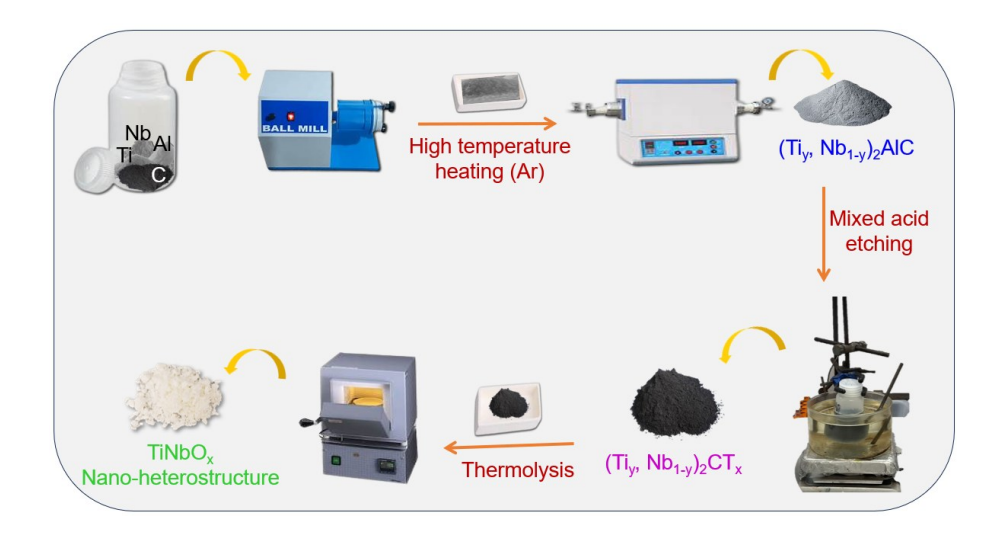


**Figure 1** Schematic representation of the preparation of TiNbO<sub>x</sub>.

### **Experimental section**

This work integrates the preparation of (Ti, Nb)<sub>2</sub>AlC (MAX phases), their corresponding MXene and oxide nano-heterostructures. Titanium (Ti, Alfa Aesar, 99.5 % metal basis, ~325 mesh), niobium (Nb, Thermo scientific, 99.8 % metal basis, ~325 mesh), aluminum (Al, Thermo scientific, 99.5 % metal basis, ~325 mesh) and carbon powder (Alfa Aesar, 99 % C, 0.2 % ash, graphite powder, APS-7-11 micron).

## Synthesis of TiNbOx

First, the MAX phase powders were prepared by mixing Ti, Nb, Al, and C powders in a stochiometric molar ratio to prepare (Ti<sub>0.75</sub>Nb<sub>0.25</sub>)<sub>2</sub>AlC, (Ti<sub>0.5</sub>Nb<sub>0.5</sub>)<sub>2</sub>AlC and (Ti<sub>0.25</sub>Nb<sub>0.75</sub>)<sub>2</sub>AlC. An excess of 0.2 Al was used to compensate for any evaporation during heating. The mixture was subjected to mixing at 56 rpm for 3 h in the presence of 20 yttria-stabilized zirconia balls of 10 mm diameter in a Turbula T2F mixer. Then, the powders were transferred to an alumina boat, inserted inside a tube furnace, and heated at 1500 °C for 3 h with a heating rate of 10 °C min<sup>-1</sup> under a continuous flow argon (Ar) 0.4 mL min<sup>-1</sup>. The obtained powders were referred to as MAX phase powders.

For the synthesis of (Ti<sub>0.25</sub>Nb<sub>0.75</sub>)<sub>2</sub>CT<sub>x</sub> MXene, 1.0 g of (Ti<sub>0.25</sub>Nb<sub>0.75</sub>)<sub>2</sub>AlC powder was slowly added to a 10 mL aqueous hydrofluoric acid solution (HF, Thermo scientific, ACS reagent, 48-51 % solution in water) solution placed in an ice bath to avoid overheating due to exothermic reactions. The mixture solution was stirred in an oil bath at 40 °C for 72 h. For (Ti<sub>0.75</sub>Nb<sub>0.25</sub>)<sub>2</sub>CT<sub>x</sub> and (Ti<sub>0.5</sub>Nb<sub>0.5</sub>)<sub>2</sub>CT<sub>x</sub>, a similar approach was followed but using a mixture of HF (48-51%) and hydrochloric acid (HCl, Thermo scientific, for analysis, 37 % solution) acids in a volume ratio of 60:40 at continuous stirring at 25 °C for 30 h. After etching, the powders, acids, and DI water were transferred to centrifuge tubes and centrifuged at 3500 rpm for 2 min. The supernatant acid was removed, and the washing procedure was repeated to reach pH 7. The settled powders in the centrifuging tubes were extracted using DI water, and the dispersion was vacuum-filtered and dried at room temperature.

The oxidized MXenes (TiNbO<sub>x</sub>) were prepared by heat treatment of the corresponding 1.0 g MXene in an alumina crucible with dimensions  $100 \times 40 \times 40$  mm in a muffle furnace at 900 °C for 1 h in air with a heating rate of 5 °C min<sup>-1</sup>. The obtained white color powders were characterized and utilized to investigate them for photocatalytic applications.

#### Photocatalytic setups and related analyses

The prepared TiNbO<sub>x</sub> powders were tested for the photocatalytic degradation of sulfamethoxazole (SMX, Merck, VETRANAL®, analytical standard) under UVA light (1.5 mW cm<sup>-2</sup> in the wavelength range 335-380 nm) in a batch mode. A double walled cylindrical pyrex container of volume 100 mL capacity was used and thermostated at 20 °C to minimize thermal effects. In each experiment, 0.2 g L<sup>-1</sup> of photocatalysts was added to 50 mL of 50 μM SMX solution in deionized water; the reaction mixture was stirred in the dark for 20 min to attain the adsorption-desorption equilibrium before irradiation at room temperature. The degradation extents were determined at fixed time intervals by sampling out 500 μL from the solution that was filtered using a polytetrafluoroethylene (PTFE) microfilter with a pore size

of 0.45  $\mu$ m and quenched into 100  $\mu$ L of methanol to stop the degradation reaction. The collected samples were analyzed by high-performance liquid chromatography (HPLC, Merck AS-2000 L-6200A L-4250) equipped with a C18 column (Hypersil Gold, 5  $\mu$ m, 150 mm × 4.6 mm; Thermo Fisher Scientific). The mobile phase was a mixture of MeOH: H<sub>2</sub>O (50:50) at a flow rate of 1 mL min<sup>-1</sup> in isocratic mode. The detection wavelength was set at 268 nm. Reactive species were identified indirectly by adding a scavenger to the reactive mixture. Tertbutanol (10 mM) scavenger was used to quench hydroxyl radicals ('OH),<sup>38</sup> and their quantification was performed by fluorescence spectrophotometer (Shimadzu RF-6000) using coumarin as probe molecule since their reaction forms 7-hydroxy coumarin (with a yield of 4.6%) which is fluorescent ( $\lambda_{ex} = 325$  nm;  $\lambda_{em} = 425$  nm).<sup>39</sup>

### **Characterizations**

The crystalline phase identification and purity was carried out using X-ray diffraction (XRD) equipped with Cu  $K_{\alpha}$  X-ray diffractometer (Rigaku D/Max-2200) at a 20 step size of 0.02° and sweep rate of 1° min<sup>-1</sup>. Crystal lattice details were gathered using Le Bail refinements and GSAS software. And Raman spectroscopy measurements were conducted using a home-built setup to obtain information about the chemical structure and molecular interactions. The measurements were performed in a backscattering configuration excited with a solid-state green laser ( $\lambda = 532$  nm). To reach the ultra-low frequency Raman shift of 10 cm<sup>-1</sup>, we used the volume Bragg grating filters to block the laser line. The backscattered signal was collected through a 100× objective and dispersed by an 1800 g/mm grating before the liquid nitrogencooled charge-coupled device (Princeton Instruments, PyLoN 1340 × 400 pixels CCD). Fourier Transform Infrared Spectroscopy (FTIR, Vertex 70v, Bruker) with diamond Attenuated total reflectance (ATR) accessory was complementary used for chemical analysis. The infrared spectra of all samples were recorded in the mid-IR range of 4000-400 cm<sup>-1</sup> with a spectral resolution of 4 cm<sup>-1</sup>. The recorded spectra are the mean of 32 scans. Before spectra acquisition

a background spectrum (air) was measured with the same parameters. OPUS software was used for background correction and transformation to the resulted absorbance spectra of samples. Scanning electron microscopy (SEM, Hitachi S-4800, at 20 kV) equipped with energy dispersive X-ray spectroscopy (EDS, ULTIM MAX 170, Oxford, at 20 kV) and transmission electron microscopy (double corrected TEM, JEOL JEM ARM 200 cF with cold field emission gun) including high-resolution transmission electron microscopy (HRTEM), bright field scanning transmission electron microscopy (SEI STEM) and selected area electron diffraction (SAED) patterns were performed to provide further details on the structure and morphology of the samples. A large angle JEOL JED-2300T CENTURIO SDD (silicon drift) detector with a solid angle of up to 0.98 sr and a detection area of 100 mm<sup>2</sup> was used for Energy Dispersive X-ray Spectroscopy (EDX) analysis. For the TEM study, powder samples were dispersed in ethanol, suspensions were sonicated for 10 min and dropped on a Cu-grid covered with holey carbon film. After drying in the air, they were examined by TEM, working at 200 kV.

The surface chemistry was studied by X-ray photoelectron spectroscopy (XPS) using an AXIS supra spectrometer. An X-ray Al Kα source (15 mA and 15 kV) generating a monochromatic beam of photons of energy 1486.6 eV was used. The charging of the samples was compensated using an automatic electron-flood gun system. The wide and core-level spectra were acquired at pass energies of 160 eV and 20 eV, respectively. The measurements were performed at 2 spots on the sample. The pressure in the working chamber was in the order of 10<sup>-7</sup> Pa. The measured data were analyzed by CasaXPS software. The spectra were referenced using the C 1s signal at 284.8 eV corresponding to C-C bonds. The background signal was subtracted by the Shirley algorithm. The synthetic components of C 1s spectra were assigned and fitted based on parameters proposed by Biesinger et al. The Ti 2p spectra were fitted based on the

parameters discussed by Biesinger et al.<sup>44</sup> The components of Nb 3d spectra were assigned based on the NIST database.<sup>45</sup> The fit of Nb 3d spectra was performed using symmetrical mixed Gaussian-Lorentzian components.

The surface area measurements were recorded using BET (Brunauer-Emmet-Teller method, Sorptomatic 1990 SERIES, Thermo Quest CE Instruments, Italy) in the relative pressure range  $p/p_0 = 0.05$ -0.25. Adsorption-desorption isotherms were measured at  $p/p_0$ =0-1, with the low-temperature adsorption method of  $N_2$  at its boiling point of 77.7 K from vacuum to atmospheric pressure. The optical properties of the samples were measured by UV-visible diffuse reflectance spectroscopy (DRS) using PerkinElmer Lambda-35 with a 50 mm integrating sphere and utilizing BaSO<sub>4</sub> as an external reference. The measured reflectance spectra were transformed by the Kubelka-Munk algorithm, and the Tauc plot was applied to determine the band gap energy ( $E_g$ ) based on the work.<sup>46</sup>

#### Results and discussion

The formation of the three different MAX phase powders, i.e.,  $(Ti_{0.75}Nb_{0.25})_2AlC$ ,  $(Ti_{0.50}Nb_{0.5})_2AlC$ , and  $(Ti_{0.25}Nb_{0.75})_2AlC$ , was confirmed based on XRD patterns and they can be indexed successfully in hexagonal symmetry with  $P6_3/mmc$  space group. A remarkable shift in XRD patterns towards lower angles with increasing Nb content from 25 to 75% was observed (Figure 2a). That was expected because of the larger atomic radius of Nb compared to Ti. The XRD patterns of corresponding MXenes (obtained after acid etching of MAX phase powders) displayed intense (002) reflections with a significant shift towards lower angles, indicating the enlargement of interlayer spacing due to surface functionalization and extraction of the Al layer (Figure 2b). The splitting of the (002) reflection might be due to the presence of water molecules intercalated between the MXene layers.

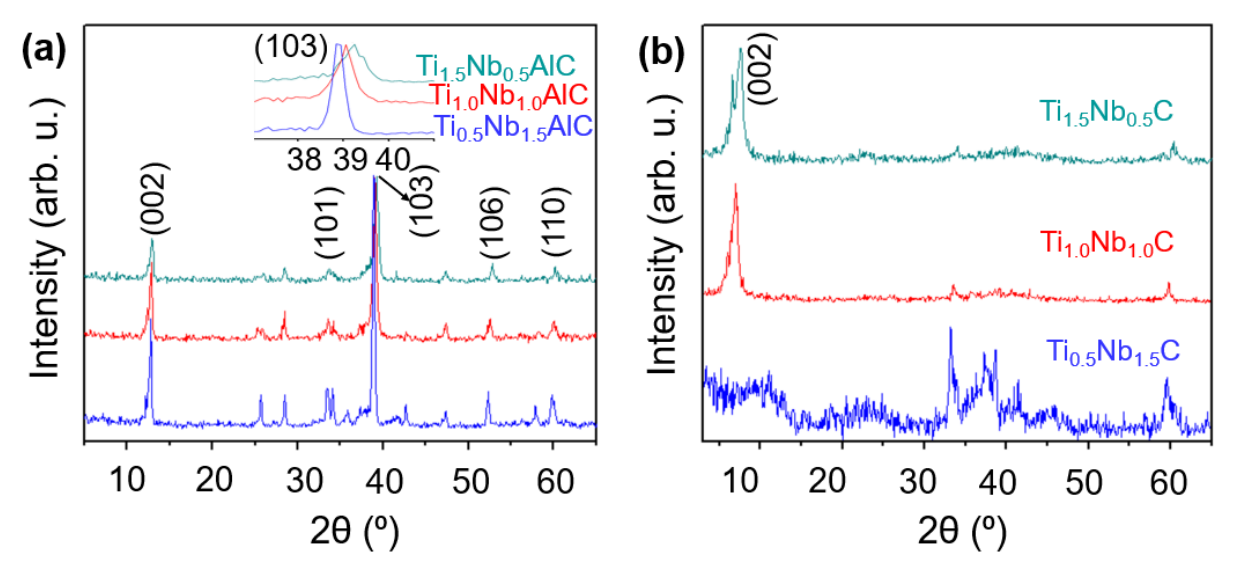


Figure 2 XRD patterns of Nb-substituted binary (a) MAX phases and (b) MXene powders. Inset in (a) shows the zoomed region from  $2\theta$  of 37 to  $41^{\circ}$ .

Further, the elemental composition of the MXenes was observed by EDS analysis, where stoichiometric Ti: Nb atomic ratios of 1.52:0.48, 1.04:0.96 and 0.55:1.45 were observed for  $(Ti_{0.75}Nb_{0.25})_2CT_x$ ,  $(Ti_{0.5}Nb_{0.5})_2CT_x$  and  $(Ti_{0.25}Nb_{0.75})_2CT_x$ , respectively, with nearly total removal of Al (Table S1). The corresponding oxidized MXenes referred to as TiNbO<sub>x</sub>-1:3, TiNbO<sub>x</sub>-1:1, and TiNbO<sub>x</sub>-3:1 (depending on the initial nominal Ti: Nb ratio in the parent MXenes) in further discussions, where the observed characteristics are linked to the photocatalytic activity of the different TiNbO<sub>x</sub>.

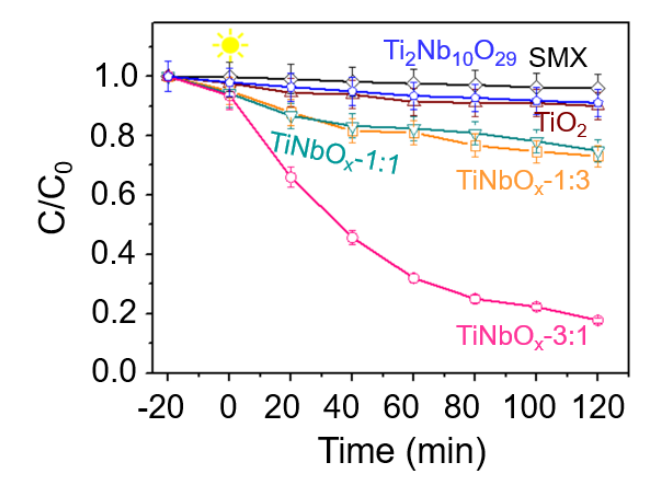


Figure 3 Degradation curves of SMX under UVA in the presence of TiNbO<sub>x</sub> powders for 2 h.

Figure 3 summarizes the performance of three TiNbO<sub>x</sub> in the degradation of SMX. For comparison purposes, the photocatalytic activity of TiO<sub>2</sub> and Ti<sub>2</sub>Nb<sub>10</sub>O<sub>29</sub> obtained by oxidation of pristine binary Ti<sub>2</sub>CT<sub>x</sub> and Nb-sustituted quaternary Nb<sub>3.5</sub>Ti<sub>0.5</sub>C<sub>3</sub>T<sub>x</sub>, respectively, and the direct photolysis of SMX is also presented in Figure 3. The TiO<sub>2</sub>- and Ti<sub>2</sub>Nb<sub>10</sub>O<sub>29</sub>-derived MXene can degrade up to 10%, while the TiNbO<sub>x</sub> powders exhibited much higher photocatalytic activity, especially TiNbO<sub>x</sub>-3:1, with 83% of SMX degradation after 2 h under UVA light. The remarkable photocatalytic behavior of the ternary oxide nano-heterostructures derived from (Ti<sub>y</sub>, Nb<sub>1-y</sub>)<sub>2</sub>CT<sub>x</sub> MXene is as follows: TiNbO<sub>x</sub>-3:1 > TiNbO<sub>x</sub>-1:1 > TiNbO<sub>x</sub>:1-3 > TiO<sub>2</sub>. Among the three oxide nano-heterostructures, the reusability behavior of the best sample i.e., TiNbO<sub>x</sub>-3:1, was examined through five consecutive cycles, and the photocatalytic efficiency in the SMX degradation slightly decreased from 83% to 72% (Figure S1), thus indicating its potential application in wastewaters treatment plants.

#### Relationship between $TiNbO_x$ properties and their photocatalytic activity

The observed trend of TiNbO<sub>x</sub> photocatalysts in SMX degradation depends on several factors, such as the crystalline phase composition, morphology, surface properties, and electronic band structure. The photocatalytic activities are discussed based on these factors to provide a detailed relationship between these properties.

### Role of crystalline phase composition and morphology

MXenes' thermal treatment in air resulted in their oxidation and formation of  $TiNbO_x$  (Figure 4a and Figure S2a). Based on reported literature, the oxidation of MXenes such as  $Ti_3C_2T_x$  and  $Ti_2CT_x$  is accompanied by the evolution of CO and  $CO_2$ , which positively impacts the porosity of the oxidized material, thus being beneficial for its photocatalytic properties. <sup>50</sup> The

XRD patterns of TiNbO<sub>x</sub> revealed the formation of rutile TiO<sub>2</sub> and monoclinic Ti<sub>2</sub>Nb<sub>10</sub>O<sub>29</sub> (Figure 4a). The reflections observed at the following 2θ values: 23.28°, 25.05°, 26.07°, 27.43, and 28.46° exhibited a shift towards lower angles with increasing Nb content, attributable to larger ionic radius of Nb than Ti (Figure 4b). A detailed study of the oxidized MXenes was also gathered by performing Le Bail refinements (Figure S2). The lattice dimensions demonstrated an increase in the cell volume of rutile TiO2 and monoclinic Ti2Nb10O29 (Table S2) that can be ascribed to the insertion of Nb into the crystal system of the MXene precursor. Moreover, the inferences of Le Bail refinements and the relative intensity ratio method (by considering w/w %, Figure S2) suggested that the major phase was rutile TiO<sub>2</sub> (82.34 %) along with Ti<sub>2</sub>Nb<sub>10</sub>O<sub>29</sub> (17.66 %) for TiNbO<sub>x</sub>-3:1 while Ti<sub>2</sub>Nb<sub>10</sub>O<sub>29</sub> (62.15 %) was predominant in TiNbO<sub>x</sub>-1:3 with competing phase of rutile TiO<sub>2</sub> (37.85 %). In TiNbO<sub>x</sub>-1:1, 60.89 % TiO<sub>2</sub> and 39.11 % Ti<sub>2</sub>Nb<sub>10</sub>O<sub>29</sub> were estimated. The Raman spectra of TiNbO<sub>x</sub>-3:1, TiNbO<sub>x</sub>-1:1, and TiNbO<sub>x</sub>-1:3 displayed characteristics bands of Ti<sub>2</sub>Nb<sub>10</sub>O<sub>29</sub> at 998 and 896 cm<sup>-1</sup> that correspond to stretching vibrations of NbO<sub>6</sub> octahedron while the bands observed at 549 and 641 cm<sup>-1</sup> could be assigned to metal-O stretching vibrations of TiO<sub>6</sub> octahedron (Figure S3).<sup>51</sup> In addition, the intense band depicted at 265 cm<sup>-1</sup> indicated symmetric and antisymmetric bending vibrations of O-Ti-O and O-Nb-O bridge bonds. 51 The intense bands observed at 617, 445, and 167 cm<sup>-1</sup> are the fingerprints of rutile TiO<sub>2</sub>.<sup>52</sup> Thus, Raman spectra inferences are consistent with XRD results. The structure of TiNbO<sub>x</sub> samples was examined using FTIR spectroscopy (Figure S4). Two absorptions occurring at 503 and 915 cm<sup>-1</sup> can be assigned to the stretching vibrations of the terminal Nb-O bond and bridging Nb-O-Nb bond. 35,53 The peaks observed at 665 and ~ 793 cm<sup>-1</sup> are the fingerprints of Ti-O-Ti and Nb-O-Nb bridging bonds.<sup>53</sup> Based on these structural analyses, it can be suggested that the photocatalytic activity of the three samples is due to the presence of transition metal oxides that are known photocatalysts, especially TiO<sub>2</sub>, since the composite with the highest ratio in Ti, leading to the highest efficiency in the photocatalytic degradation of SMX.<sup>54</sup> However, the TiO<sub>2</sub> obtained from the oxidation of Ti<sub>2</sub>CT<sub>x</sub> MXene exhibited the lowest photocatalytic activity, thus suggesting that the composite formed an efficient heterojunction.

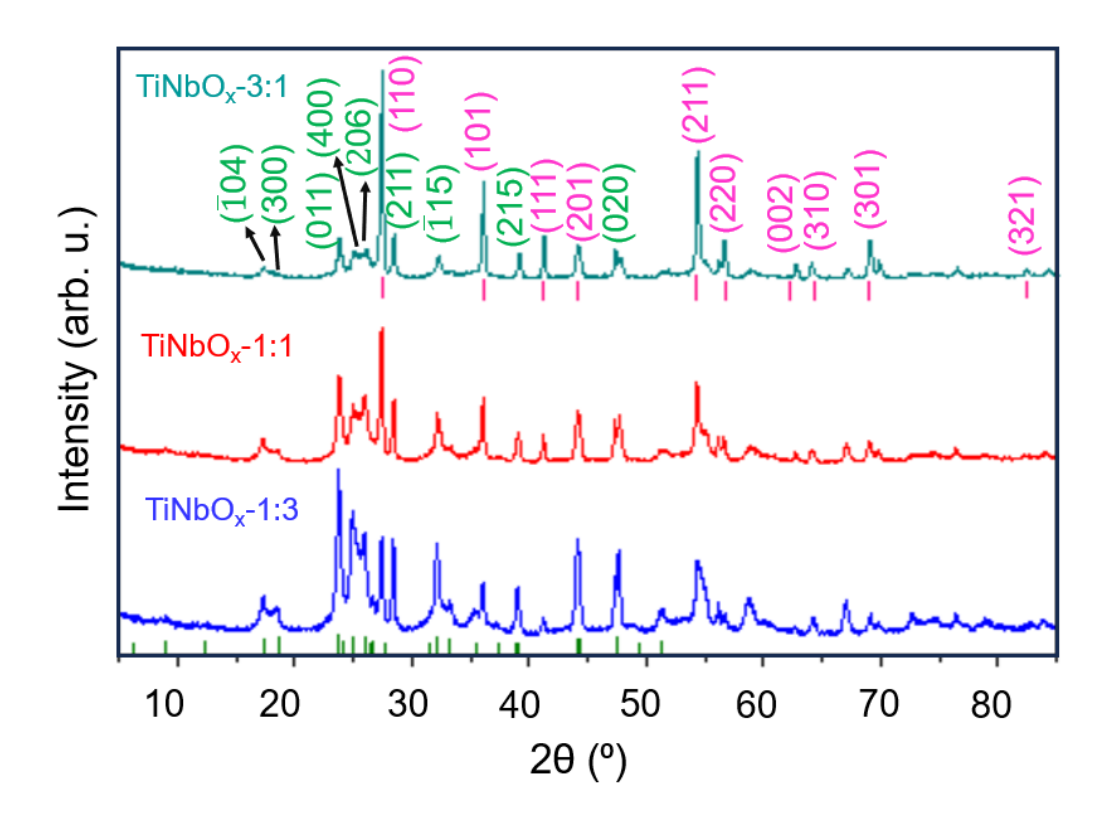


**Figure 4** XRD patterns of the complete oxidation of Nb-substituted binary MXenes in air. Reflection marked in pink represents rutile TiO<sub>2</sub> (PDF#00-001-1292) and in green corresponds to monoclinic Ti<sub>2</sub>Nb<sub>10</sub>O<sub>29</sub> (PDF#00-040-0039).

The multilayered structure of the oxidized MXene seems to be intact after oxidation, and this phenomenon might arise due to insufficient oxidation (Figure 5).<sup>29</sup> Indeed, during the formation and stabilization of TiO<sub>2</sub> and Ti<sub>2</sub>Nb<sub>10</sub>O<sub>29</sub>, there might be a surface functionalization with carbon moieties, facilitating the conservation of the layered arrangements.<sup>29</sup> Table S3 confirms the unchanged stoichiometry between Ti: Nb in MXene precursors and TiNbO<sub>x</sub>, with significant remaining carbon based on EDS analysis.

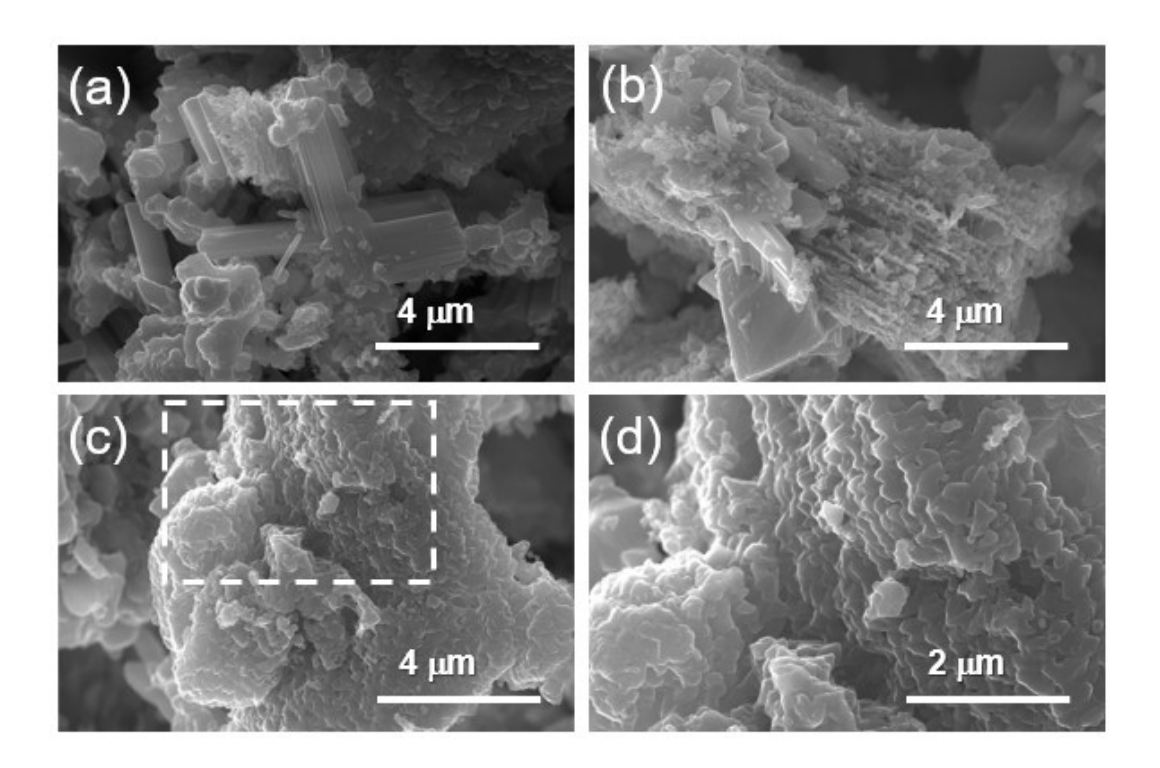


**Figure 5** SEM images of (a)  $TiNbO_x$ -1:3, (b)  $TiNbO_x$ -1:1, (c)  $TiNbO_x$ -3:1, and (d) zoomed region of  $TiNbO_x$ -3:1.

The TEM results for TiNbO<sub>x</sub> can provide crucial information in relation to photocatalytic activity (Figure 6 and Figure S5-S7). In the case of TiNbO<sub>x</sub>-1:3, a mesoporous nanosheet-like structure with sizes up to  $10~\mu m$  is observed, and these nanosheets originate by the interconnection of nanoparticles' sizes from 50-150 nm in a porous network (Figure 6a).

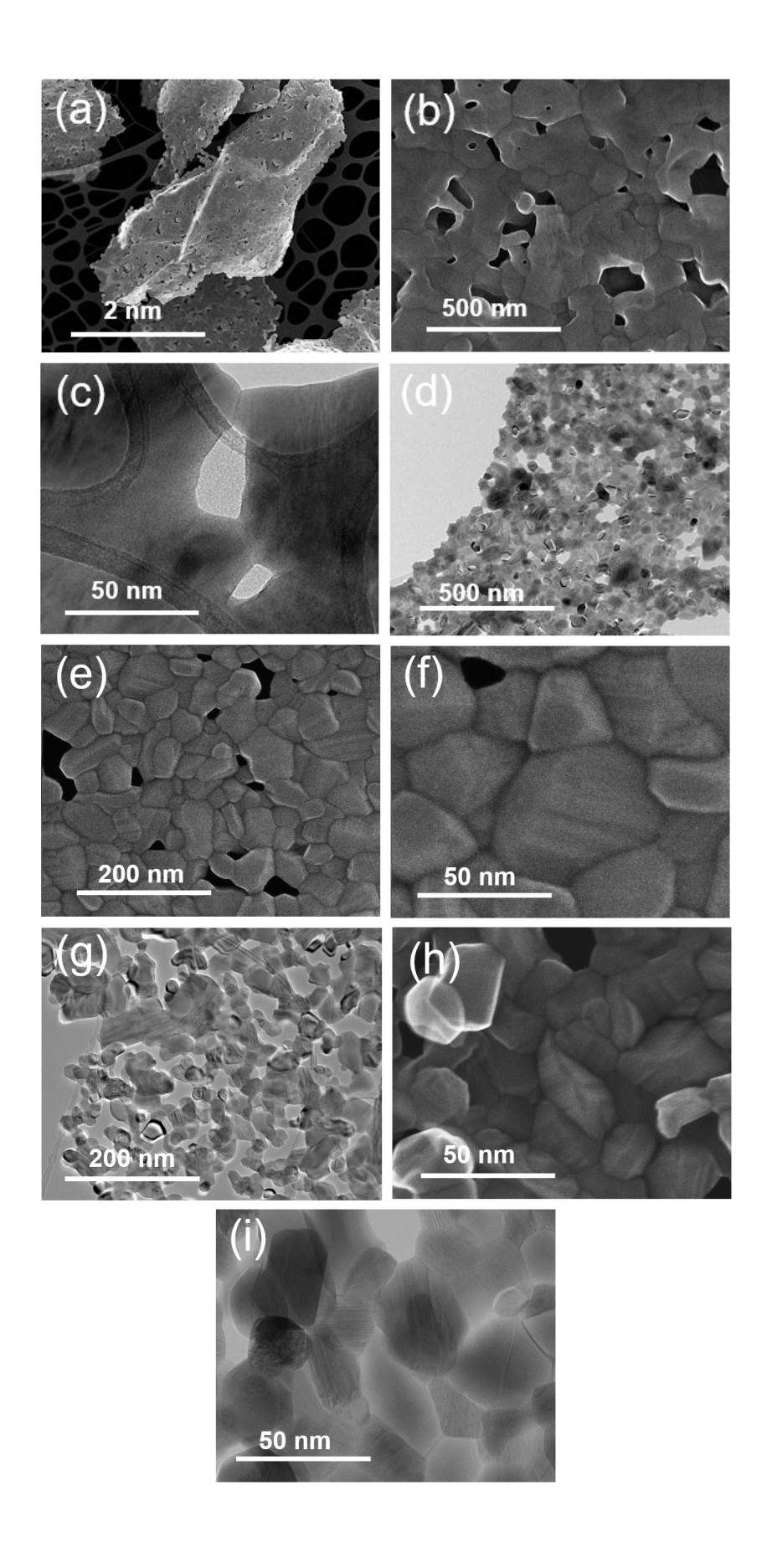


**Figure 6** SEI STEM (a, b, e, f, and h) and BF STEM (c, d, g, and i) images of sheet-like objects at different magnifications for (a-c) TiNbO<sub>x</sub>-1:3, (d-f) TiNbO<sub>x</sub>-1:1 and (g-i) TiNbO<sub>x</sub>-3:1 sample.

A better view of the fusion of the nano-sized crystallites in nanosheets and in interconnected fashion can be seen in Figure 6b-6c. Similarly, TiNbO<sub>x</sub>-1:1 consists of mesoporous nanosheets but with densely packed crystallites with sizes in the range of 40-85 nm and high porosity (Figure 6d-6f). Concerning TiNbO<sub>x</sub>-3:1, the mesoporous nanosheet-like structure with densely packed particles is also observed with smaller particle sizes (between 40-70 nm) and larger porosity (Figure 6g-6i). We believe that the larger porosity in the TiNbO<sub>x</sub>-3:1 sheet could be related to the breakdown of the delaminated nanolayers into smaller aggregates of nanoparticles (Figure 6g).

HRTEM imaging and EDS mapping of Ti, Nb, and O elements showed that sheets in TiNbO<sub>x</sub>-3:1 and TiNbO<sub>x</sub>-1:1 consist of TiO<sub>2</sub> and Ti<sub>2</sub>Nb<sub>10</sub>O<sub>29</sub> mixture (Figure S6 and S7), while sheets in TiNbO<sub>x</sub>-1:3 sample are consisted of majorly Ti<sub>2</sub>Nb<sub>10</sub>O<sub>29</sub> phase and exhibited uniform distribution of Ti and Nb (Figure S5). From the evaluation of the FFT pattern in Figure S5d, it was determined that Ti<sub>2</sub>Nb<sub>10</sub>O<sub>29</sub> crystallite was oriented along [21] direction, but crystallite exhibiting [010] zone axis was also revealed, as shown in Figure S4f. EDS maps of Ti and Nb obtained from TiNbO<sub>x</sub>-1:1 and TiNbO<sub>x</sub>-3:1 samples revealed an inhomogeneous distribution of Ti and Nb elements in nanosheets (Figure S6a and S7a), which indicates that TiO<sub>2</sub> and Ti<sub>2</sub>Nb<sub>10</sub>O<sub>29</sub> nanograins are organized into sheet-like structures. While TiO<sub>2</sub> nanocrystals significantly prevailed over Ti<sub>2</sub>Nb<sub>10</sub>O<sub>29</sub> in sample TiNbO<sub>x</sub>-3:1, the proportion of TiO<sub>2</sub> and Ti<sub>2</sub>Nb<sub>10</sub>O<sub>29</sub> approximately coincided with a ratio of 40:60 in the sample TiNbo<sub>x</sub>-1:1 (Figure S6a). The presence of rutile and Ti<sub>2</sub>Nb<sub>10</sub>O<sub>29</sub> nanoparticles in the heterojunction sheet-like material was also accounted for from their HRTEM and respective FFT patterns (Figure S6c,

d, e, f). Figure 5c exhibits the BF STEM image of TiO<sub>2</sub> rutile crystal (dark) viewed along the [010] direction surrounded by Ti<sub>2</sub>Nb<sub>10</sub>O<sub>29</sub> single crystals, thus confirming heterojunction formation in TiNbO<sub>x</sub>. Nano-heterostructure TiO<sub>2</sub>/Ti<sub>2</sub>Nb<sub>10</sub>O<sub>29</sub> emerges where the coexistence of TiO<sub>2</sub> (marked R) and Ti<sub>2</sub>Nb<sub>10</sub>O<sub>29</sub> grains is inferred from the HRTEM method (Figure S6b). Detailed HRTEM image of Ti<sub>2</sub>Nb<sub>10</sub>O<sub>29</sub> with respective FFT pattern exhibiting zone axis of [211] is presented in Figure S6e, f. It explains why TiNbO<sub>x</sub> is more efficient than TiO<sub>2</sub> in the photocatalytic degradation of SMX (Figure 3).

Among all three samples, TiNbO<sub>x</sub>-3:1 possesses a higher porosity and smaller crystallite sizes, resulting in increased surface-active sites, favoring its higher photocatalytic activity. The HRTEM images of the three TiNbO<sub>x</sub>, along with the corresponding FFT or SAED patterns, confirmed the presence of TiO<sub>2</sub> and Ti<sub>2</sub>Nb<sub>10</sub>O<sub>29</sub> (Figure S5-S7), thus supporting the XRD data As seen from Figure S6c, d and Figure S7c, d, rutile crystals in nanosheets of TiNbO<sub>x</sub>-1:1 and TiNbO<sub>x</sub>-3:1 samples are well faceted. By evaluating the FFT pattern, Figure S7d, gained from Figure S7c, a rutile single crystal is enclosed by combining the {110} and {101} type planes, which are prismatic and pyramidal facets, respectively. The same result is also shown in Figure S6c, d. The presence of an oxidation preferred faces of {101} type and the reduction preferred faces of {110} type enclosing the nanocrystals in the TiNbO<sub>x</sub>-3:1 sample with the highest proportion of rutile TiO<sub>2</sub> can support the high photocatalytic activity of TiNbO<sub>x</sub>-3:1.<sup>55</sup> Furthermore, the appearance of nano twins and voids in rutile nanocrystals of TiNbO<sub>x</sub>-3:1 (Figure S7e, f) is responsible for elevating free charge transfer as well as facilitates the separation of charge carriers, which further may help in boosting photocatalytic activity.<sup>56</sup> These morphological features may support the photocatalytic behavior since TiNbO<sub>x</sub>-3:1 is the most efficient sample in the degradation of SMX.

BET analysis of the samples are provided in Table 1. The data predominantly showed the macro-mesoporous nature of the TiNbO<sub>x</sub> samples. However, micropores in the TiNbO<sub>x</sub>-3:1

sample suggested its multiscale porosity. Indeed, materials with multiscale porosity are highly desirable as they can improve overall photocatalytic efficiency by enhancing the mass transfer of molecules into solids and light utilization efficiency.<sup>57</sup> TiNbO<sub>x</sub>-3:1 has a significantly higher surface area, further supporting its higher photocatalytic activity for SMX degradation.

**Table 1** Characteristic parameters for TiNbO<sub>x</sub> obtained from BET analysis.

Sample identification	a [m²/g]	b [cm <sup>3</sup> /g]	c [cm <sup>3</sup> /g]	d [cm <sup>3</sup> /g]	e [cm³/g]	f
	[m /g]	[CIII /g]	[CIII /g]	[CIII /g]	[CIII /g]	C ME MI
TiNbO <sub>x</sub> -1:3	+0.5	+0.11	0.011	0	0.025	few ME, no MI,
						with multiple MA
TiNbO <sub>x</sub> -1:1	+0.3	+0.06	0.007	0	0.010	few ME, no MI,
						with multiple MA
TiNbO <sub>x</sub> -3:1	+4	+1.0	0.014	0.001	0.021	little ME, less MI,
						with more MA

a – specific surface area according to BET<sup>58</sup> - marked+; b – volume of the adsorbed monomolecular layer; c – cumulative pore volume according to Gurvich; d – cumulative volume of micropores (MI) according to Horvath-Kawazoe; e – cumulative volume of mesopore (ME) and macropore (MA) according to BJH method; f – nature of the material.

### Role of surface chemistry

The materials' photocatalytic efficiency is generally intricately linked to their surface chemistry. The wide spectra (Figure S8) documented the presence of O, C, Nb, and Ti elements on the surface of the TiNbO<sub>x</sub> samples. To further elucidate the surface chemistry, we thoroughly analyzed core-level spectra of C 1s, Ti 2p, and Nb 3d orbitals presented in Figure 7. Notably, the XPS detects the signal from a 2-10 nm depth below the surface. The C 1s spectra of the samples (Figure 7a, d, and g) consist of components at positions 284.8 eV. 286.3, 287.8 eV, and 288.8 eV of binding energy ascribed to C-C (or C-H), C-O (or C-O-C). C=O, and O-C=O species, coressponding to adventitious carbon contaminants.<sup>59</sup> The relative share of the components in C 1s spectra was very similar among the TiNbO<sub>x</sub> samples (Table S4). Therefore, the formation of carbon species on the surface was not affected by the stoichiometry of oxidized MXenes. It is known that the hydrophilic groups on the surface (C-O, C=O, O-C=O) of photocatalysts can enhance photocatalytic activity due to improved interaction with organic pollutants.<sup>60</sup>

Nevertheless, the higher photocatalytic performance of the TiNbO<sub>x</sub>-3:1 sample compared to the other counterparts cannot be explained by these detected hydrophilic groups since their ratio are very similar for them (Table S4). The Ti 2p spectra (Figure 7b, e, and h) comprised the doublet lines Ti 2p<sub>3/2</sub> and Ti 2p<sub>1/2</sub> at a binding energy of 458.7 eV and 464.4 eV, respectively. The doublet line splitting of 5.7 eV and the positions of the components reflect the presence of Ti ions in oxidation state +IV. This supports the structure of Ti<sub>2</sub>Nb<sub>10</sub>O<sub>29</sub> and the presence of TiO<sub>2</sub>,<sup>61</sup>detected by XRD within the bulk area of the samples. The Nb 3d corelevel spectra of the TiNbO<sub>x</sub> samples (Figure 7c, f, and i) show the doublet lines Nb 3d<sub>5/2</sub> and Nb 3d<sub>3/2</sub> at a binding energy of 207.1 eV and 209.8 eV. The deconvolution of the spectra to the corresponding components reflects the presence of Nb in oxidation state +V, corresponding to Ti<sub>2</sub>Nb<sub>10</sub>O<sub>29</sub>.<sup>35,42</sup>

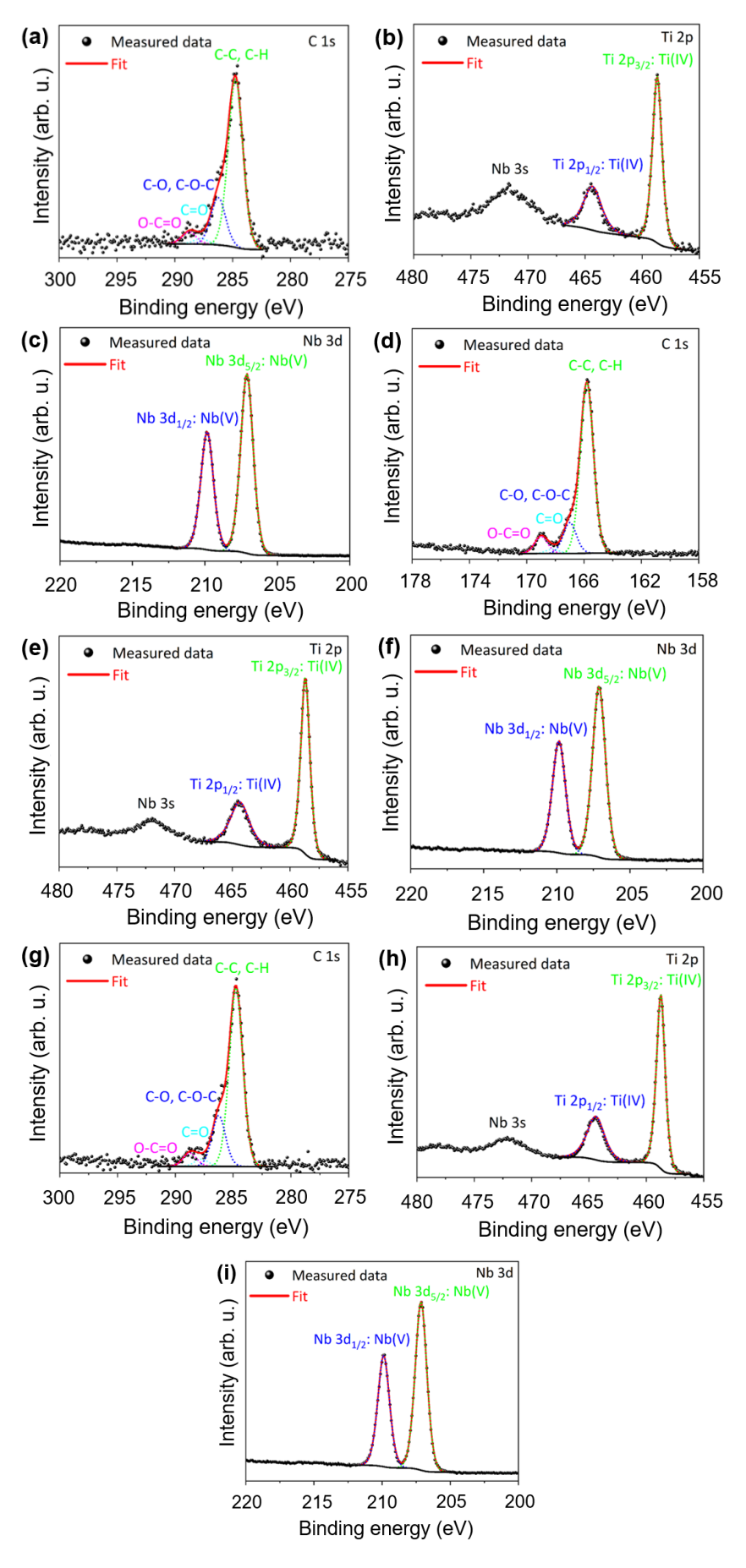


**Figure 7** The XPS C 1s, Ti 2p, and Nb 3d core-level spectra of TiNbO<sub>x</sub>-1:3 (a)-(c), TiNbO<sub>x</sub>-1:1 (d)-(f), and TiNbO<sub>x</sub>-3:1 (g)-(i). The spectra are referenced using C-C, C-H peak at 284.8 eV.

#### Role of the electronic bandstructure

Figure 8 displays the UV-visible DRS spectra of the TiNbO<sub>x</sub> samples. A red shift was observed with decreasing Nb-content in TiNbO<sub>x</sub>, i.e., UV to the visible region (Figure 8a). The optical band gap (E<sub>g</sub>) energy decreases as the Nb content decreases. By assuming an indirect energy band gap for plotting the Tauc's plots, the estimated E<sub>g</sub> is as the following: TiNbO<sub>x</sub>-1:3 > TiNbO<sub>x</sub>-1:1 > TiNbO<sub>x</sub>-3:1 with corresponding values of 3.10, 3.01 and 2.87 eV (Figure 8b).<sup>62</sup> Based on XPS studies, we detected similar surface chemistry in samples; therefore, we assume the high photocatalytic behavior of TiNbO<sub>x</sub>-3:1 primarily can be attributed to bulk properties rather than surface characteristics. TiO<sub>2</sub> is well known to exhibit higher photocatalytic activity when enriched with bulk or volume defects instead of surface defects.<sup>63</sup> Based on TEM analysis (Figure S7f), the exceptional behavior of TiNbO<sub>x</sub>-3:1 may originate from the presence of volume defects as voids within the TiO<sub>2</sub> nanocrystal.<sup>64</sup> Additionally, a narrower energy band gap will lead to higher utilization of solar light, i.e., in both the UVA and visible regions.

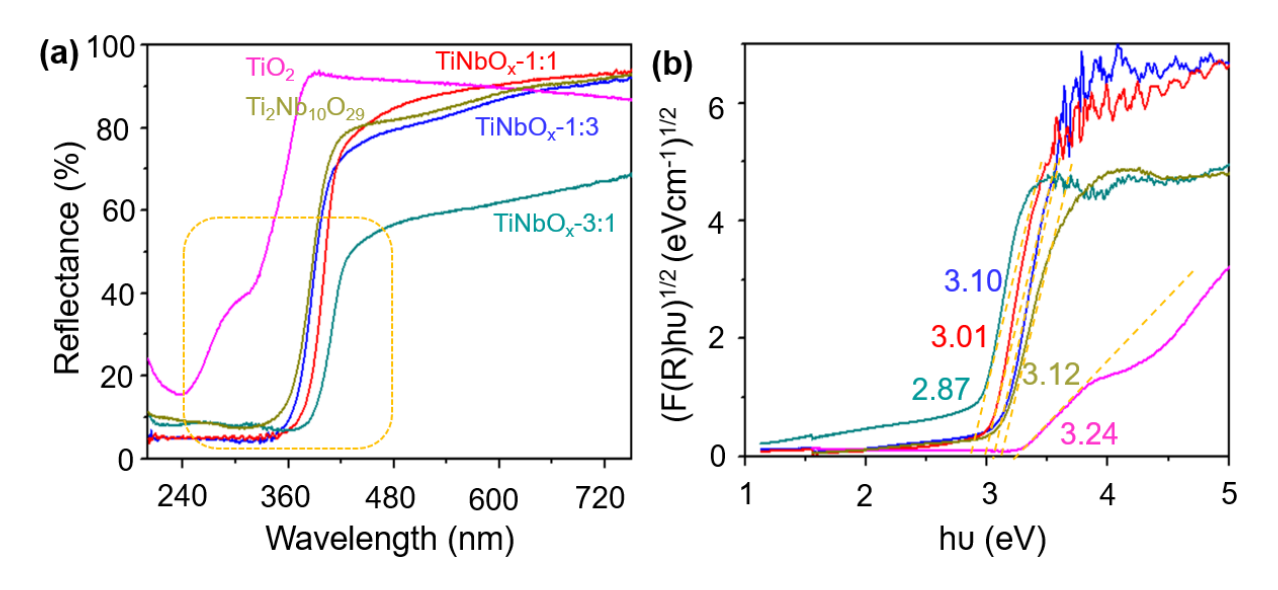


**Figure 8** (a) UV-visible DRS of TiO<sub>2</sub>, Ti<sub>2</sub>Nb<sub>10</sub>O<sub>29</sub>, TiNbO<sub>x</sub> samples and their corresponding (b) band gap plots.

The TiNbO<sub>x</sub> samples have been found to exhibit a reduced band gap compared to pure rutile TiO<sub>2</sub> (3.24 eV) and monoclinic Ti<sub>2</sub>Nb<sub>10</sub>O<sub>29</sub> (3.12 eV) phases derived by the oxidation of Ti<sub>2</sub>CT<sub>x</sub> and Nb<sub>3.5</sub>Ti<sub>0.5</sub>C<sub>3</sub>T<sub>x</sub> and it might be due to structural defects brought by the synthesis method as explained above. In addition, the valence band maximum of the TiNbOx analyzed by UV photoelectron spectroscopy has been calculated at 2.90 eV (Figure S9).<sup>65</sup> Therefore, the electronic band structure of TiNbO<sub>x</sub> can be reasonably estimated as a heterojunction type II (Figure 9).<sup>66,67,68</sup> Such a heterojunction will favor the charge carrier's separation, where photogenerated electrons are accumulated in TiO<sub>2</sub> and photogenerated holes in Ti<sub>2</sub>Nb<sub>10</sub>O<sub>29</sub> under UVA illumination (Figure 9). This is the one main reason why TiNbO<sub>x</sub> exhibited higher photocatalytic efficiency than TiO<sub>2</sub>. Among the TiNbO<sub>x</sub> samples, the highest photocatalytic activity is observed for TiNbO<sub>x</sub>-3:1, probably because rutile TiO<sub>2</sub> (the predominant phase in this sample) is more photoactive than Ti<sub>2</sub>Nb<sub>10</sub>O<sub>29</sub>.<sup>69</sup>

#### Proposed photocatalytic mechanism

The photocatalytic processes using TiO<sub>2</sub>-based materials are usually accompanied by the generation of reactive oxygen species (ROS) such as 'OH and O<sub>2</sub>-, from which hydroxyl radical is the predominant one.<sup>70,71</sup> Indeed, superoxide anion radicals can be converted to H<sub>2</sub>O<sub>2</sub> and ultimately into 'OH.<sup>72</sup> To detect 'OH, coumarin has been used as a probe molecule since it forms 7-hydroxycoumarin (7OH-C) (with a yield of 4.6 %),<sup>42</sup> which can be easily detectable by using a fluorescence spectrophotometer. The amount of 'OH formation for TiNbO<sub>x</sub>-3:1 was twice and thrice that of TiNbO<sub>x</sub>-1:1 and TiNbO<sub>x</sub>-1:3 (Figure S10), which supports its higher photocatalytic activity in the degradation of SMX.

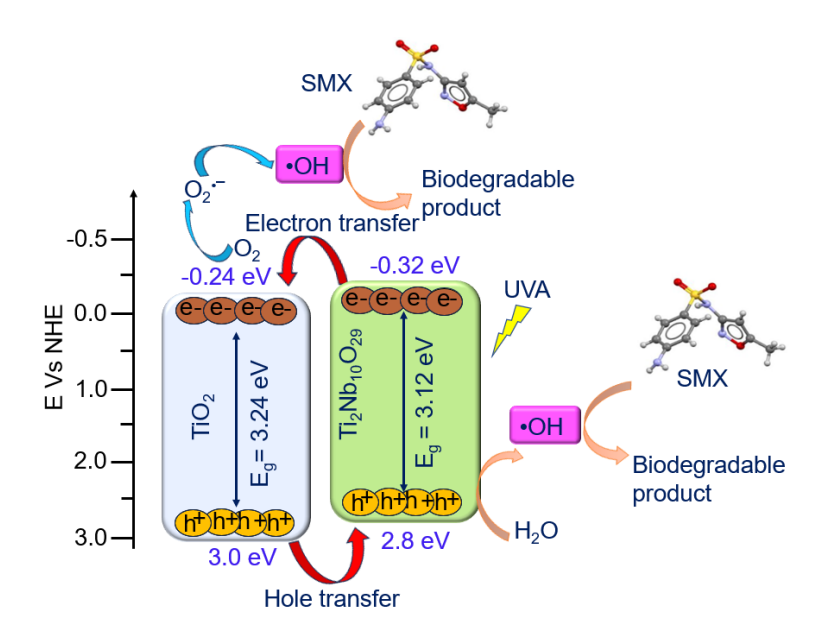


Figure 9 Proposed mechanism of SMX photocatalytic degradation by using TiNbO<sub>x</sub>.

Further, t-butanol was employed as a selective scavenger for 'OH during photocatalytic measurements, and the results showed a complete quench of the photocatalytic degradation of SMX (Figure S10), which implied 'OH is the predominant ROS involved in the degradation reactions. Based on the estimated electronic band structure of TiNbO<sub>x</sub>, the mechanism of SMX degradation is proposed. The lower photocatalytic activity of TiNbO<sub>x</sub>-1:1 and TiNbO<sub>x</sub>-1:3 in the SMX degradation can be correlated with the concentration of TiO<sub>2</sub>. As per the estimated electronic band structure, under UVA irradiation, e<sup>-</sup> are accumulated in TiO<sub>2</sub> and h<sup>+</sup> in Ti<sub>2</sub>Nb<sub>10</sub>O<sub>29</sub> by following eqn. (1). The higher photocatalytic activity of TiNbO<sub>x</sub>-3:1, is accompanied by generation of large number of 'OH, by interaction of h<sup>+</sup> with H<sub>2</sub>O/OH<sup>-</sup> and e<sup>-</sup> with adsorbed O<sub>2</sub> molecule on the surface of catalyst by following eqn. (2-5).<sup>73</sup>

$$TiNbO_{x} \xrightarrow{hv} h^{+} + e^{-}$$
 (1)

$$h^+ + H_2O \rightarrow {}^{\bullet}OH + H^+ \tag{2}$$

$$e^- + O_2 \rightarrow O_2^{\bullet -} \tag{3}$$

$$O_2^{\bullet -} + H^+ \to HO_2^{\bullet} \tag{4}$$

$$HO_2^{\bullet} + HO_2^{\bullet} \longrightarrow H_2O_2 + O_2 \tag{5}$$

$$H_2O_2 \xrightarrow{hv} 2 \text{ 'OH}$$
 (6)

Notably, the pure TiO<sub>2</sub> and Ti<sub>2</sub>Nb<sub>10</sub>O<sub>29</sub> derived from the oxidation of MXenes exhibited the weakest activity in SMX degradation. It confirmed the importance of Nb-substitution in binary MXenes, which are precursors to preparing innovative photocatalysts. Compared to other reported studies which are mainly focused on dye degradation (Table S5), the current work highlights the significance of our findings since innovative oxide heterostructures composed of Ti and Nb oxides are efficient photocatalyst for the degradation of SMX which is considered a PAC. Since all the TiNbO<sub>x</sub> samples are composed of type-II heterojunction with similar surface chemistry and layered morphology derived from their MXene precursor, the higher superior photocatalytic activity of TiNbOx-3:1 is attributed to its higher porosity and higher Ti:Nb ratio in TiO<sub>2</sub>, thus leading to an efficient production of \*OH.

#### **Conclusions**

For the first time, innovative oxide nano-heterostructures were prepared by oxidizing Ti-Nb MXenes, and their photocatalytic performance in the degradation of SMX under UVA light was evaluated. Among the three tested TiNbO<sub>x</sub> samples composed of TiO<sub>2</sub> and Ti<sub>2</sub>Nb<sub>10</sub>O<sub>29</sub>, TiNbO<sub>x</sub>-3:1 exhibited the best degradation performance. The complex interplay between the structural, morphological, and electronic properties of TiNbO<sub>x</sub> suggested that a higher Ti:Nb ratio, smaller particle size, and larger specific surface area were the key factors contributing to its superior photocatalytic performance. This study underscores the complex influence of structural, morphological, and electronic properties on the photocatalytic properties of TiNbO<sub>x</sub>. Moreover, the proposed degradation mechanism invoves 'OH as the primary ROS, getting produced in significantly high amounts in the presence of TiNbO<sub>x</sub>-3:1. The primary conclusion

emerging from the present work illustrates TiNbO<sub>x</sub>-3:1 as an efficient oxide nano-

heterostructure photocatalyst, which can be explored further in wastewaters treatment.

**Conflicts of Interest** 

There are no conflicts to declare.

Acknowledgments

This work has been carried out in the frame of the PhotoMXene project No. 3305/03/02, co-

funded by the EU Horizon 2020 Research and Innovation Program under the Program

SASPRO2 COFUND Marie Sklodowska-Curie grant agreement No. 945478. Materials

synthesis and characterization at Tulane University was supported by the US National Science

Foundation (NSF) CAREER Project DMR-2048164. This work was also partially financed by

the Slovak Research and Development Agency under the contract No. APVV-21-0039. This

research was supported by projects LM2023039 and LM2023051, funded by the Ministry of

Education, Youth and Sports of the Czech Republic.

**CRediT** statement

Shalu Atri: Conceptualization – Investigation – Methodology – Writing: original draft –

Writing: review & editing – Funding acquisition

Elham Loni: Investigation – Methodology – Writing: review & editing

Frantisek Zazimal: Investigation – Methodology – Writing: review & editing

**Karol Hensel**: Investigation – Methodology.

Maria Caplovicova: Investigation – Methodology.

Gustav Plesch: Supervision.

25

**Xin** Lu: Investigation – Methodology.

Rajamani Nagarajan: Investigation- Methodology- Writing: review and editing

**Michael Naguib**: Conceptualization – Supervision –Writing: review & editing – Funding acquisition.

**Olivier Monfort**: Conceptualization – Supervision – Writing: original draft – Writing: review & editing – Funding acquisition.

#### References

- [1] Wang, H. J., Li, X., Zhao, X. X., Li, C. Y., Song, X. H., Zhang, P., Huo, P. W., Li, X., Research progress on semiconductor photocatalysts and their modification strategies for environmental remediation. *Chin. J. Catal.* 2022, *43* (2), 178.
- [2] Guo, Z., Zhou, J., Zhu, L., Sun, Z., MXene: a promising photocatalyst for water splitting. *J. Mater. Chem.*, A 2016. 4(29), 11446-11452.
- [3] Shen, R., Xie, J., Xiang, Q., Chen, X., Jiang, J., Li, X. Ni-based photocatalytic H<sub>2</sub>-production cocatalysts<sub>2</sub>. *Chin. J. Catal.* 2019 *40*(3), 240-288.
- [4] Zhao, Y., Li, Z., Li, M., Liu, J., Liu, X., Waterhouse, G. I., Wang, Y., Zhao, J., Gao, W., Zhang, Z., Long, R. Reductive transformation of layered-double-hydroxide nanosheets to Febased heterostructures for efficient visible-light photocatalytic hydrogenation of CO. *Adv. Mater.* 2018, *30*(36), 1803127.
- [5] Li, X., Yu, J., Jaroniec, M., Chen, X. Cocatalysts for selective photoreduction of CO<sub>2</sub> into solar fuels. *Chem. Rev.* 2019, *119*(6), 3962-4179.
- [6] Fan, Y., Ma, W., Han, D., Gan, S., Dong, X., Niu, L., Convenient recycling of 3D AgX/graphene aerogels (X= Br, Cl) for efficient photocatalytic degradation of water pollutants. *Adv. Mater.* 2015, *27*(25), 3767-3773.

- [7] Khaki, M. R. D., Shafeeyan, M. S., Raman, A. A. A., Daud, W. M. A. W. Application of doped photocatalysts for organic pollutant degradation-A review. *J. Environ. Manag.* 2017, 198, 78-94.
- [8] Nikokavoura, A., Trapalis, C. Alternative photocatalysts to TiO<sub>2</sub> for the photocatalytic reduction of CO<sub>2</sub>. *Appl. Surf. Sci.* 2017, *391*, 149-174.
- [9] Karkman, A., Do, T. T., Walsh, F. Virta, M. P. Antibiotic-resistance genes in wastewater. *Trends Microbiol.* 2018, *26*(3), .220-228.
- [10] Wu, Z., Song, W., Xu, X., Yuan, J., Lv, W., Yao, Y. High 1T phase and sulfur vacancies in C-MoS<sub>2</sub>@ Fe induced by ascorbic acid for synergistically enhanced contaminants degradation. *Sep. Purif. Technol.* 2022, *286*, 120511.
- [11] Fujishima, A., Honda, K. Electrochemical photolysis of water at a semiconductor electrode. *Nature* 1972, *238*(5358), 37-38.
- [12] Chen, X., Mao, S. S. Titanium dioxide nanomaterials: synthesis, properties, modifications, and applications. *Chem. Rev.* 2007, *107*(7), 2891-2959.
- [13] Wang, Y., Ding, Z., Arif, N., Jiang, W. C., Zeng, Y. J. 2D material based heterostructures for solar light-driven photocatalytic H<sub>2</sub> production. *Mater. Adv.* 2022, *3*(8), 3389-3417.
- [14] Su, Q., Li, Y., Hu, R., Song, F., Liu, S., Guo, C., Zhu, S., Liu, W., Pan, J., Heterojunction photocatalysts based on 2D materials: the role of configuration. *Adv. Sustain. Syst.* 2020, *4*(9), 2000130.
- [15] Zhang, Z., Yates Jr, J. T. Band bending in semiconductors: chemical and physical consequences at surfaces and interfaces. *Chem. Rev.* 2012, *112*(10), 5520-5551.
- [16] Wang, H., Zhang, L., Chen, Z., Hu, J., Li, S., Wang, Z., Liu, J., Wang, X. Semiconductor heterojunction photocatalysts: design, construction, and photocatalytic performances. *Chem. Soc. Rev.* 2014, *43*(15), 5234-5244.

- [17] Naguib, M., Barsoum, M. W., Gogotsi, Y. Ten years of progress in the synthesis and development of MXenes. *Adv. Mater.* 2021, *33*(39), 2103393.
- [18] Naguib, M., Kurtoglu, M., Presser, V., Lu, J., Niu, J., Heon, M., Hultman, L., Gogotsi, Y., Barsoum, M. W. Two-dimensional nanocrystals produced by exfoliation of Ti<sub>3</sub>AlC<sub>2</sub>. *Adv. Mater.* 2011, *23*(37), 4248-4253.
- [19] Sherryna, A., Tahir, M. Role of surface morphology and terminating groups in titanium carbide MXenes (Ti<sub>3</sub>C<sub>2</sub>T<sub>x</sub>) cocatalysts with engineering aspects for modulating solar hydrogen production: A critical review. *Chem. Eng. J.* 2022, *433*, 134573.
- [20] Wang, Y., Chen, J., Que, M., Wu, Q., Wang, X., Zhou, Y., Ma, Y., Li, Y., Yang, X. MXene-derived Ti<sub>3</sub>C<sub>2</sub>Tx/Bi<sub>4</sub>Ti<sub>3</sub>O<sub>12</sub> heterojunction photocatalyst for enhanced degradation of tetracycline hydrochloride, rhodamine B, and methyl orange under visible-light irradiation. *Appl. Surf. Sci.* 2023, *639*, 158270.
- [21] Das Chakraborty, S., Kumar, U., Bhattacharya, P., Mishra, T. Tailoring of Visible to Near-Infrared Active 2D MXene with Defect-Enriched Titania-Based Heterojunction Photocatalyst for Green H<sub>2</sub> Generation. *ACS Appl. Mater. Interfaces* 2024, *16*(2),2204-2215.
- [22] Zhang, Q., Teng, J., Zou, G., Peng, Q., Du, Q., Jiao, T., Xiang, J. Efficient phosphate sequestration for water purification by unique sandwich-like MXene/magnetic iron oxide nanocomposites. *Nanoscale* 2016, 8(13), 7085-7093.
- [23] Ahmed, B., Anjum, D. H., Hedhili, M. N., Gogotsi, Y., Alshareef, H. N. H<sub>2</sub>O<sub>2</sub> assisted room temperature oxidation of Ti<sub>2</sub>C MXene for Li-ion battery anodes. *Nanoscale* 2016, 8(14), 7580-7587.
- [24] Zheng, T., Wang, W., Du, Q., Wan, X., Jiang, Y., Yu, P. 2D Ti3C2-MXene Nanosheets/ZnO Nanorods for UV Photodetectors. *ACS Appl. Nano Mater.* 2024.
- [25] Shah, N., Wang, X., Tian, J. Recent advances in MXenes: a promising 2D material for photocatalysis. *Mater. Chem. Front.* 2023, 7(19), 4184-4201.

- [26] Sun, B., Lu, S., Qian, Y., Zhang, X., Tian, J. Recent progress in research and design concepts for the characterization, testing, and photocatalysts for nitrogen reduction reaction. *Carbon Energy* 2023, *5*(3), e305.
- [27] Fang, B., Xing, Z., Sun, D., Li, Z., Zhou, W. Hollow semiconductor photocatalysts for solar energy conversion. *Adv. Powder Mater.* 2022, *I*(2), 100021.
- [28] Jia, G., Wang, Y., Cui, X., Zheng, W. Highly carbon-doped TiO<sub>2</sub> derived from MXene boosting the photocatalytic hydrogen evolution. *ACS Sustain. Chem. Eng.* 2018, 6(10), 13480-13486.
- [29] Naguib, M., Mashtalir, O., Lukatskaya, M. R., Dyatkin, B., Zhang, C., Presser, V., Gogotsi, Y., Barsoum, M. W. One-step synthesis of nanocrystalline transition metal oxides on thin sheets of disordered graphitic carbon by oxidation of MXenes. *ChemComm.* 2014, *50*(56), 7420-7423.
- [30] Tang, T., Wang, Z., Guan, J. Electronic structure regulation of single-site MNC electrocatalysts for carbon dioxide reduction. *Acta Phys.-Chim. Sin.* 2022, *39*, 10-3866.
- [31] Husmann, S., Besch, M., Ying, B., Tabassum, A., Naguib, M., Presser, V. Layered titanium niobium oxides derived from solid-solution Ti-Nb carbides (MXene) as anode materials for Li-ion batteries. *ACS Appl. Energy Mater.* 2022, *5*(7), 8132-8142.
- [32] Kajbafvala, A., Ghorbani, H., Paravar, A., Samberg, J. P., Kajbafvala, E., Sadrnezhaad, S. K. Effects of morphology on photocatalytic performance of Zinc oxide nanostructures synthesized by rapid microwave irradiation methods. *Superlattices Microstruct*.2012, *51*(4), 512-522,
- [33] Ouyang, S., Li, Z., Ouyang, Z., Yu, T., Ye, J., Zou, Z. Correlation of crystal structures, electronic structures, and photocatalytic properties in a series of Ag-based oxides: AgAlO<sub>2</sub>, AgCrO<sub>2</sub>, and Ag<sub>2</sub>CrO<sub>4</sub>. *J. Phys. Chem.*, C 2008, 112(8), 3134-3141.

- [34] Wang, H. Y., Chen, J., Xiao, F. X., Zheng, J., Liu, B. Doping-induced structural evolution from rutile to anatase: formation of Nb-doped anatase TiO<sub>2</sub> nanosheets with high photocatalytic activity. *J. Mater. Chem.*, A 2016, 4(18), 6926-6932.
- [35] Xie, M., Zhu, H., Fang, M., Huang, Z., Liu, Y. G., Wu, X. Band-gap engineering and comparative investigation of Ti<sub>2</sub>Nb<sub>10</sub>O<sub>29</sub> photocatalysts obtained by various synthetic routes. *Appl. Surf. Sci.* 2018, *435*, 39-47.
- [36] Adhami, T., Ebrahimi-Kahrizsangi, R., Bakhsheshi-Rad, H.R., Majidi, S., Ghorbanzadeh, M., Berto, F. Synthesis and electrochemical properties of TiNb<sub>2</sub>O<sub>7</sub> and Ti<sub>2</sub>Nb<sub>10</sub>O<sub>29</sub> anodes under various annealing atmospheres. *Metals* 2021, *11*(6), 983.
- [37] Fatima, M., Fatheema, J., Monir, N.B., Siddique, A.H., Khan, B., Islam, A., Akinwande, D., Rizwan, S. Nb-doped MXene with enhanced energy storage capacity and stability. *Front. Chem.* 2020, *8*, 168.
- [38] Jia, D., Monfort, O., Hanna, K., Mailhot, G., Brigante, M. Caffeine degradation using peroxydisulfate and peroxymonosulfate in the presence of Mn<sub>2</sub>O<sub>3</sub>. Efficiency, reactive species formation, and application in sewage treatment plant water. *J. Clean. Prod.* 2021, *328*, 129652.
- [39] Marion, A., Brigante, M., Mailhot, G. A new source of ammonia and carboxylic acids in cloud water: The first evidence of photochemical process involving an iron-amino acid complex. *Atmos. Environ.* 2018, *195*, 179-186.
- [40] Von Dreele, R. B., Larson, A. C. General structure analysis system (GSAS). *Los Alamos Natl. Lab. Rep. LAUR* 2004, 748, 86-748.
- [41] Toby, B. H. EXPGUI, a graphical user interface for GSAS. J. Appl. Crystallogr. 2001, 34(2), 210-213.
- [42] Fairley, N., Fernandez, V., Richard-Plouet, M., Guillot-Deudon, C., Walton, J., Smith, E., Flahaut, D., Greiner, M., Biesinger, M., Tougaard, S., Morgan, D. Systematic and collaborative

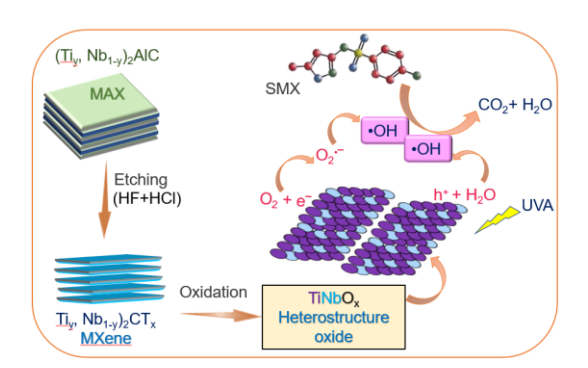
- approach to problem-solving using X-ray photoelectron spectroscopy. *Appl. Surf. Sci. Adv.* 2021, 5, 100112.
- [43] Biesinger, M. C. Accessing the robustness of adventitious carbon for charge referencing (correction) purposes in XPS analysis: Insights from a multi-user facility data review. *Appl. Surf. Sci.* 2022, *597*, 153681.
- [44] Biesinger, M. C., Lau, L. W., Gerson, A. R., Smart, R. S. C. Resolving surface chemical states in XPS analysis of first-row transition metals, oxides and hydroxides: Sc, Ti, V, Cu and Zn. *Appl. Surf. Sci.* 2010, *257*(3), 887-898.
- [45] Naumkin, A. V., Kraut-Vass, A., Gaarenstroom, S. W., Powell, C. J. NIST X-ray Photoelectron Spectroscopy Database, NIST. *Stand. Ref. Database* 2000, *20*.
- [46] Makuła, P., Pacia, M., Macyk, W. How to correctly determine the band gap energy of modified semiconductor photocatalysts based on UV-Vis spectra. *J. Phys. Chem. Lett.* 2018, 9(23), 6814-6817.
- [47] Hug, G., Jaouen, M., Barsoum, M. W. X-ray absorption spectroscopy, EELS, and full-potential augmented plane wave study of the electronic structure of Ti<sub>2</sub>AlC, Ti<sub>2</sub>AlN, Nb<sub>2</sub>AlC, and (Ti<sub>0.5</sub>Nb<sub>0.5</sub>)<sub>2</sub>AlC. *Phys. Rev.*, *B* 2005, 71(2), 024105.
- [48] Ahmed, B., Anjum, D. H., Hedhili, M. N., Gogotsi, Y., Alshareef, H. N. H<sub>2</sub>O<sub>2</sub> assisted room temperature oxidation of Ti<sub>2</sub>C MXene for Li-ion battery anodes. *Nanoscale* 2016, *8*(14), 7580-7587.
- [49] Lotfi, R., Naguib, M., Yilmaz, D. E., Nanda, J., Van Duin, A. C. A comparative study on the oxidation of two-dimensional Ti<sub>3</sub>C<sub>2</sub> MXene structures in different environments. *J. Mater. Chem.*, A 2018, 6(26), 12733-12743.
- [50] Atri, S., Malik, V., Uma, S., Nagarajan, R. Catalytic applications of mesoporous CaBi<sub>2</sub>O<sub>4</sub> obtained from a single source precursor. *Res. Chem. Intermed.* 2019, *45*, 2457-2470.

- [51] Lian, Y., Zheng, Y., Wang, Z., Hu, Y., Zhao, J., Zhang, H. Hollow ppy@ Ti<sub>2</sub>Nb<sub>10</sub>O<sub>29-x</sub>@ NC bowls: a stress–release structure with vacancy defects and coating interface for Li capacitor. *Chem. Eng. J.* 2023, *454*, 140287.
- [52] Zhang, Y., Harris, C. X., Wallenmeyer, P., Murowchick, J., Chen, X. Asymmetric lattice vibrational characteristics of rutile TiO<sub>2</sub> as revealed by laser power dependent Raman spectroscopy. *J. Phys. Chem.*, C 2013, 117(45), 24015-24022.
- [53] Lou, S., Cheng, X., Gao, J., Li, Q., Wang, L., Cao, Y., Ma, Y., Zuo, P., Gao, Y., Du, C., Huo, H. Pseudocapacitive Li<sup>+</sup> intercalation in porous Ti<sub>2</sub>Nb<sub>10</sub>O<sub>29</sub> nanospheres enables ultrafast lithium storage. *Energy Stor. Mater.*, 2018, *11*, 57-66.
- [54] Djokicc, V. R., Marinkovicc, A. D., Petrovicc, R.D., Ersen, O., Zafeiratos, S., Mitricc, M., Ophus, C., Radmilovicc, V. R., Janaćkovicc, D. T. Highly active rutile TiO<sub>2</sub> nanocrystalline photocatalysts. *ACS Appl. Mater. Interfaces* 2020, *12*(29), 33058-33068.
- [55] Badovinac, I. J., Peter, R., Omerzu, A., Salamon, K., Saric, I., Samarzija, A., Percic, M., Piltaver, I.K., Ambrozic, G., Petravic, M. Grain size effect on photocatalytic activity of TiO<sub>2</sub> thin films grown by atomic layer deposition. *Thin Solid Films* 2020, 709, 138215.
- [56] Liu, H., Zhao, T., Kong, L., Cao, X., Zhu, W., Huang, Y., Bo, M. Twinning enhanced electrical conductivity and surface activity of nanostructured CuCrO<sub>2</sub> gas sensor. *Sen. Actuators B Chem.* 2021, 338, 129845.
- [57] Wang, X., Yu, J. C., Ho, C., Hou, Y., Fu, X. Photocatalytic activity of a hierarchically macro/mesoporous titania. *Langmuir* 2005, *21*(6), 2552-2559.
- [58] Brunauer, S., Emmett, P. H., Teller, E. Adsorption of gases in multimolecular layers. *J. Am. Chem. Soc.* 1938, 60(2), 309-319.

- [59] Biesinger, M. C. Accessing the robustness of adventitious carbon for charge referencing (correction) purposes in XPS analysis: Insights from a multi-user facility data review. *Appl. Surf. Sci.* 2022, *597*, 153681.
- [60] Cha, B. J., Saqlain, S., Seo, H. O., Kim, Y. D. Hydrophilic surface modification of TiO<sub>2</sub> to produce a highly sustainable photocatalyst for outdoor air purification. *Appl. Surf. Sci.* 2019, 479, 31-38.
- [61] Biesinger, M. C., Lau, L. W., Gerson, A. R., Smart, R. S. C. Resolving surface chemical states in XPS analysis of first-row transition metals, oxides and hydroxides: Sc, Ti, V, Cu and Zn. *Appl. Surf. Sci.* 2010, *257*(3), 887-898.
- [62] Aperador, W., Yate, L., Pinzon, M. J., Caicedo, J. C. Optical and semiconductive properties of binary and ternary thin films from the Nb-Ti-O system. *Results Phys.* 2018, *9*, 328-336.
- [63] Zhang, H., Cai, J., Wang, Y., Wu, M., Meng, M., Tian, Y., Li, X., Zhang, J., Zheng, L., Jiang, Z., Gong, J. Insights into the effects of surface/bulk defects on photocatalytic hydrogen evolution over TiO<sub>2</sub> with exposed {001} facets. *Appl. Catal., B Environ.* 2018, 220, 126-136. [64] Yan, J., Wu, G., Guan, N., Li, L., Li, Z., Cao, X. Understanding the effect of surface/bulk defects on the photocatalytic activity of TiO<sub>2</sub>: anatase versus rutile. *Phys. Chem. Chem. Phys.* 2013, 15(26), 10978-10988.
- [65] Das, P., Sengupta, D., Kasinadhuni, U., Mondal, B., Mukherjee, K. Nano-crystalline thin and nano-particulate thick TiO<sub>2</sub> layer: Cost-effective sequential deposition and study on dyesensitized solar cell characteristics. *Mater. Res. Bull.* 2015, 66, 32-38.
- [66] Gao, C., Wei, T., Zhang, Y., Song, X., Huan, Y., Liu, H., Zhao, M., Yu, J., Chen, X. A photoresponsive rutile TiO<sub>2</sub> heterojunction with enhanced Electron–Hole separation for high-performance hydrogen evolution. *Adv. Mater.* 2019, *31*(8), 1806596.

- [67] Lin, C., Yu, S., Zhao, H., Wu, S., Wang, G., Yu, L., Li, Y., Zhu, Z. Z., Li, J., Lin, S. Defective Ti<sub>2</sub>Nb<sub>10</sub>O<sub>27</sub>. 1: an advanced anode material for lithium-ion batteries. *Sci. Rep.* 2015, *5*(1), 17836.
- [68] Zhu, H. X., Zhou, P. X., Li, X., Liu, J. M. Electronic structures and optical properties of rutile TiO<sub>2</sub> with different point defects from DFT+ U calculations. *Phys. Lett.*, A 2014, 378(36), 2719-2724.
- [69] Rajput, R. B., Kale, R. B. Photocatalytic activity of solvothermally synthesized rutile TiO<sub>2</sub> nanorods for the removal of water contaminants. *Mater. Sci. Eng.*, B 2023, 294, 116556.
- [70] Fujishima, A., Zhang, X., Tryk, D. A. TiO<sub>2</sub> photocatalysis and related surface phenomena. *Surf. Sci. Rep.* 2008, *63*(12), 515-582.
- [71] Hirakawa, T., Nosaka, Y., Properties of O<sub>2</sub> and OH formed in TiO<sub>2</sub> aqueous suspensions by photocatalytic reaction and the influence of H<sub>2</sub>O<sub>2</sub> and some ions. *Langmuir* 2002, *18*(8), 3247-3254.
- [72] Xiao, Y., Carena, L., Nasi, M. T., Vahatalo, A. V. Superoxide-driven autocatalytic dark production of hydroxyl radicals in the presence of complexes of natural dissolved organic matter and iron. *Water Res.* 2020, *177*, 115782.
- [73] Lin, Y. T., Weng, C. H., Lin, Y. H., Shiesh, C. C., Chen, F. Y. Effect of C content and calcination temperature on the photocatalytic activity of C-doped TiO<sub>2</sub> catalyst. *Sep. Purific. Technol.* 2013, *116*, 114-123.

## **Table of Contents**



Oxide nano-heterostructures derived from MXene with macroscale porosity have been produced and tested in the photocatalytic degradation of sulfamethoxazole.